AIP Journal of Applied Physics

Production of annular electron beams by foilless diodes

R. B. Miller, K. R. Prestwich, J. W. Poukey, and S. L. Shope

Citation: Journal of Applied Physics **51**, 3506 (1980); doi: 10.1063/1.328203
View online: http://dx.doi.org/10.1063/1.328203
View Table of Contents: http://scitation.aip.org/content/aip/journal/jap/51/7?ver=pdfcov
Published by the AIP Publishing

Production of annular electron beams by foilless diodes

R. B. Miller, K. R. Prestwich, J. W. Poukey, and S. L. Shope
Sandia Laboratories, Albuquerque, New Mexico 87185

(Received 20 December 1979; accepted for publication 7 April 1980)

A number of important aspects of the production of annular electron beams by foilless diodes are examined, both theoretically and experimentally. The theories of Ott, Antonsen, and Lovelace (OAL) and Chen and Lovelace (CL) are compared, and the CL theory is extended to include the effect of an axial gap in an approximate fashion. For the case of finite magnetic field strengths, Larmor orbits are examined and radial oscillations of the beam profile are predicted from a beam envelope analysis. Experimental results obtained with both low- and high-impedance sources have been compared with the theory, and based on such studies, the design and construction of an intense hollow beam generator are described. Experimental results obtained with the new diode compare favorably with both the analytic theory and the results of numerical simulations. The device currently produces 2-MeV electrons at beam currents of 65–70 kA.

PACS numbers: 41.80.Dd

I. INTRODUCTION

For several applications, including collective particle acceleration and microwave generation, it is advantageous to generate an intense electron beam in the form of a thin annulus in order to avoid problems associated with the space-charge potential of the beam. For the general case of a uniform annular electron beam with inner and outer radii r_1 and r_2 injected with initial kinetic energy $(\gamma_0 - 1)mc^2$ into a cylindrical pipe of radius R, the space-charge limiting current is given approximately by[1]

$$I_{\mathrm{SCL}} = \frac{(\gamma_0^{2/3} - 1)^{3/2}(mc^3/e)}{1 - [2r_1^2/(r_2^2 - r_1^2)]\ln(r_2/r_1) + 2\ln(R/r_2)}. \quad (1)$$

In Eq. (1) m and e are the mass and charge of an electron and c is the speed of light. For a solid beam ($r_1 = 0$), Eq. (1) reduces to[2]

$$I_{\mathrm{SCL}} \approx \frac{(\gamma_0^{2/3} - 1)^{3/2}(mc^3/e)}{1 + 2\ln(R/r_2)}, \quad (2)$$

while for a hollow beam of thickness $a \ll r_1$, Eq. (1) becomes

$$I_{\mathrm{SCL}} \approx \frac{(\gamma_0^{2/3} - 1)^{3/2}(mc^3/e)}{a/r_1 + 2\ln(R/r_2)}. \quad (3)$$

Comparing Eqs. (2) and (3) it is apparent that if the beam is located near the drift tube wall ($r_2 \approx R$) the space-charge limit for the thin hollow beam case can be substantially higher than for the case of the solid beam.

In the generation of such high-current hollow beams, an explosive emission foilless diode should have several advantages.[3] While thermionic cathodes are source limited to current densities of $\lesssim 50$ A/cm^2,[4] a cold cathode explosively emitting a thin beam at the space-charge limit can easily produce beam current densities as high as 3×10^4 A/cm^2 without employing beam compression methods. The foilless diode configuration also eliminates the problem of anode vaporization at high current densities and beam heating due to scattering in the anode foil.

The issue of central importance for foilless diode design is to establish appropriate diode impedance scaling laws for geometries and parameter regimes of practical importance. In the following sections of this paper a number of important aspects of the production of thin hollow beams are examined, both theoretically and experimentally. Section II contains a summary of the theory of foilless diode operation, while Sec. III contains the results of experimental studies discussed with respect to the theory. Based on such results, the design and experimental testing of an intense hollow beam accelerator are described in Sec. IV. Pertinent conclusions are summarized in Sec. V.

II. THEORETICAL SUMMARY

A. Infinite magnetic field impedance models for foilless diodes

Theoretical analyses of foilless diodes have adopted the somewhat idealized geometry of Fig. 1; a semi-infinite cathode with surface potential $\phi_c(r)$ is joined at a right angle to a grounded anode. Electron emission is assumed to occur over a limited (roughened) region of the cathode surface; the electron motion is constrained to be one dimensional by a very strong applied axial magnetic field. In addition, the applied voltage is assumed to be ultrarelativistic so that the narrow cathode sheath region can be ignored. Under these assumptions a self-consistent solution for the electron current density is found which satisfies the criterion of space-charge-limited emission over the roughened portion of the cathode surface.

1. Ott, Antonsen, and Lovelace model[5]

The model of Ott, Antonsen, and Lovelace (OAL) is essentially that of a "corner diode" for which the cathode surface is maintained at a constant potential $-\phi_0$. The OAL

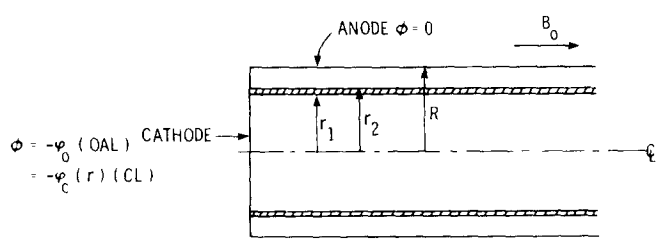

FIG. 1. Idealized geometry for the planar foilless diode.

 0021-8979/80/073506-10$01.10

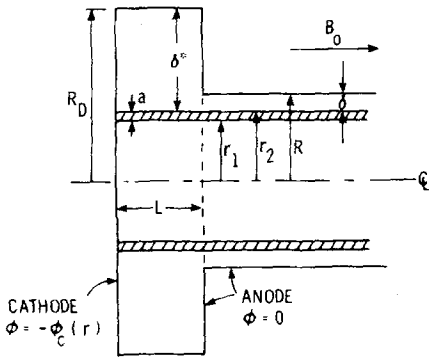

FIG. 2. Idealized geometry for the planar foilless diode with an axial gap.

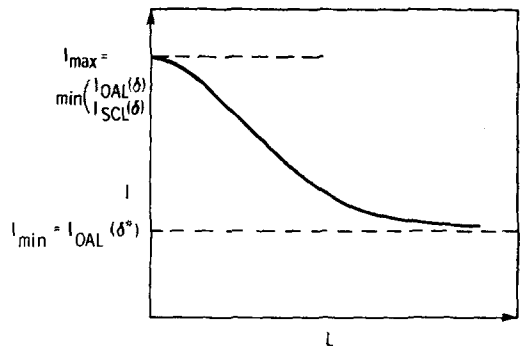

FIG. 3. Qualitative variation of foilless diode current as a function of axial gap separation.

model contains a number of interesting features: (a) It illustrates the interplay between the beam emission profile and the condition of space-charge-limited emission. Although electron emission can occur over all roughened cathode surfaces, the beam density profile is markedly hollow. (b) The diode impedance is only a weak function of the width of the emitting region because the inner emission surface is shielded by the space-charge of the electrons emitted at the outer surfaces.

For the simple limiting case of a beam which is thin compared with its distance to the anode wall δ, the diode impedance is given approximately by

$$Z \approx \frac{1}{c}\frac{\delta}{r_b}\ln\left(\frac{8\delta}{a}\right), \tag{4}$$

and the total diode current is approximately

$$I_t = (\gamma_0 - 1)(mc^3/e)\frac{r_b}{\delta}\left[\ln\left(\frac{8\delta}{a}\right)\right]^{-1}. \tag{5}$$

In this ultrarelativistic limit, the impedance is independent of the diode voltage, and increases as the beam separation from the drift tube wall increases. An *ad hoc* approximation which extends the validity of Eq. (5) to cathode potentials which are not ultrarelativistic is to replace $(\gamma_0 - 1)$ by the factor $(\gamma_0^{2/3} - 1)^{3/2}$, i.e.,

$$I_{\mathrm{OAL}} \approx (\gamma_0^{2/3} - 1)^{3/2}(mc^3/e)\frac{r_b}{\delta}\left[\ln\left(\frac{8\delta}{a}\right)\right]^{-1}. \tag{6}$$

2. Chen and Lovelace model[6]

The model of Chen and Lovelace (CL) is similar to the OAL model except that the electric potential is allowed to vary over an arbitrary boundary. In principle this permits a more accurate representation of experimental cathode geometries of interest. The solution for the potential may be written as

$$\phi(r,z) = \frac{8\pi}{R^2}\sum_{n=1}^{\infty}\frac{\rho_n}{k_n^2}(1 - e^{k_n z})\psi_n(r) + \frac{2}{R^2}\sum_{n=1}^{\infty}\phi_n e^{-k_n z}\psi_n(r), \tag{7}$$

where $\psi_n(r) = J_0(k_n r)\,[J_1(k_n R)]^{-2}$, and $k_n = \lambda_n/R$, where the λ_n are the roots of the J_0 Bessel function. The expansion coefficients are given by

$$\rho_n = \int_0^R r dr \rho(r) J_0(k_n r), \tag{8}$$

$$\phi_n = \int_0^R r dr \phi_c(r) J_0(k_n r). \tag{9}$$

The assumption of space-charge-limited emission imposes the restriction that $E_z(r,0) = 0$ over the emission surface, and in principle yields the ρ_n once the cathode surface potential $\phi_c(r)$ has been specified. The most general case of emission over an annulus defined by $r_1 < r < r_2 < R$ leads to the integral equation

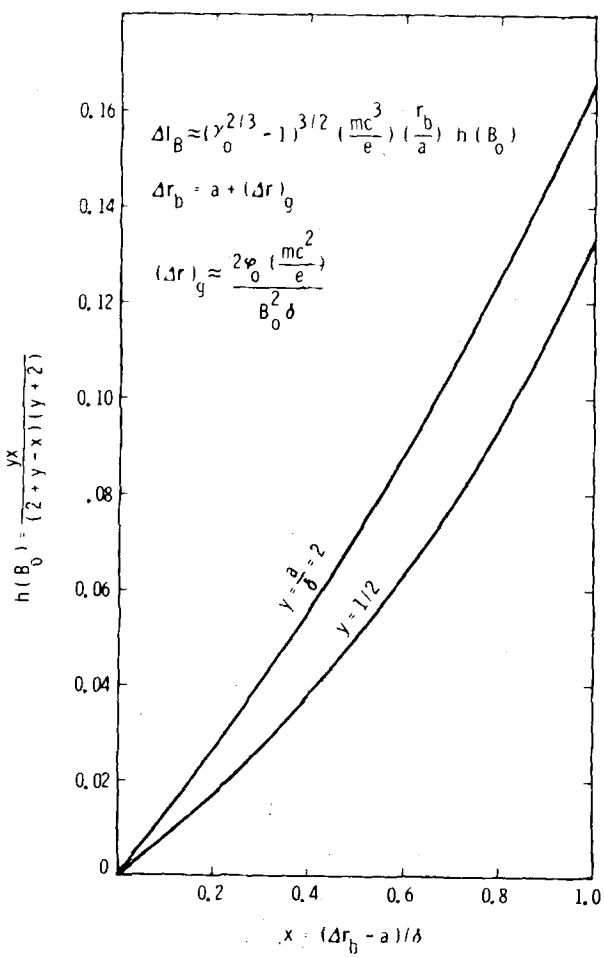

FIG. 4. Qualitative variation in foilless diode current with magnetic field strength due to variation in the beam thickness.

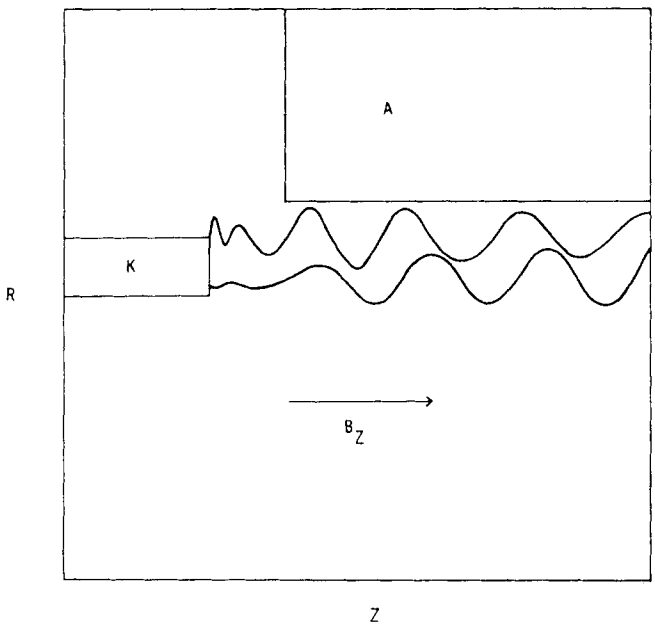

FIG. 5. Sample elctron trajectories in a foilless diode. $V = 2$ MV, B_z (applied) = 20 kG, cathode (K) radius = 1 cm, system length = 16 cm.

$$\frac{1}{4\pi}\sum_{n=1}^{\infty} k_n\phi_n\psi_n(r) = \int_{r_1}^{r_2} r^1 dr^1 K(r,r^1)\rho(r^1), \tag{10}$$

where the kernel is defined by

$$K(r,r^1) = \sum_{n=1}^{\infty}\frac{1}{k_n}\psi_n(r)J_0(k_n r^1). \tag{11}$$

Equation (10) is the basic integral equation for the cylindrical diode. It can be formally solved by expanding the Bessel functions in a set of basis functions $u_j(r)$, which are complete and orthonormal on the interval (r_1,r_2). This procedure has been carried out by CL for the special case of $r_1 \to 0$. They find that the diode behavior predicted by their model is qualitatively similar to that given by the OAL model. In particular, they find the beams are, in general, hollow. In addition, the particle kinetic energy flux is observed to increase as the beam decreases, in accord with intuitive space-charge arguments.

3. Longitudinal gap effects

In several instances it is desirable to control the impedance by varying the axial separation between the cathode tip and the smaller cylindrical drift region. Using the CL formalism it is possible to obtain approximate expressions for the diode current and impedance which include the axial gap separation. For the idealized geometry of Fig. 2, the appropriate Green's function is

$$G(r,z|r^1,z^1) = \frac{8\pi}{R_D^2}\sum_{n=1}^{\infty}\frac{J_0(k_n r)J_0(k_n r^1)}{k_n[J_1(k_n R_D)]^2\sinh(k_n L)} \times \begin{cases}\sinh(k_n z)\sinh[k_n(L-z^1)], & z<z^1\\ \sinh[k_n(L-z)]\sinh(k_n z^1), & z>z^1.\end{cases} \tag{12}$$

Expanding the charge density and the cathode potential in terms of Bessel functions [Eqs. (8) and (9) with R replaced by R_D], and performing the necessary integrations yield

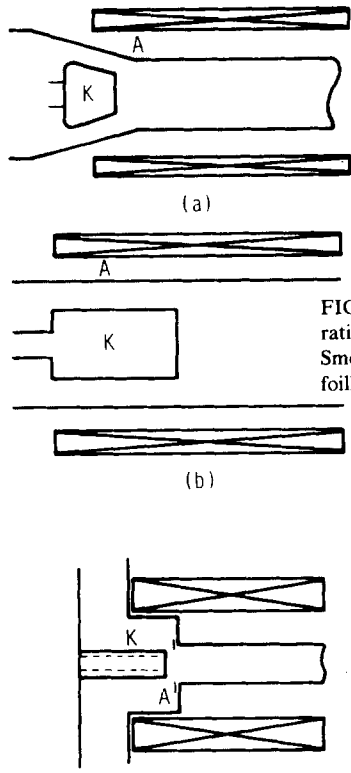

FIG. 6. Various foilless diode configurations: (a) Friedman diode. (b) Smooth bore magnetron. (c) Planar foilless diode.

$$\phi(r,z) = \frac{16\pi^2}{R_D^2}\sum_{n=1}^{\infty}\frac{\rho_n J_0(k_n r)}{k_n^2[J_1(\lambda_n)]^2\sinh(k_n L)} \times (\sinh[k_n(L-z)][\cosh(k_n z)-1] + \sinh(k_n z)\{\cosh[k_n(L-z)]-1\}) + \frac{4\pi}{R_D^2}\sum_{n=1}^{\infty}\frac{\phi_n J_0(k_n r)}{[J_1(\lambda_n)]^2\sinh(k_n L)}\sinh[k_n(L-z)]. \tag{13}$$

Assuming space-charge-limited emission over the "roughened" annulus $r_1 < r < r_2$ leads to the integral equation

$$\frac{1}{4\pi}\sum_{n=1}^{\infty}\frac{k_n\phi_n\psi_n}{\sinh(k_n L)}\cosh(k_n L) = \int_{r_1}^{r_2} r^1 dr^1 K_L(r,r^1)\rho(r^1), \tag{14}$$

where the kernel $K_L(r,r^1)$ for the longitudinal gap is given by

$$K_L(r,r^1) = \sum_{n=1}^{\infty}\frac{\psi_n(r)J_0(k_n r^1)}{k_n\sinh(k_n L)}[\cosh(k_n L)-1]. \tag{15}$$

In the strong magnetic field limit, the foilless diode with

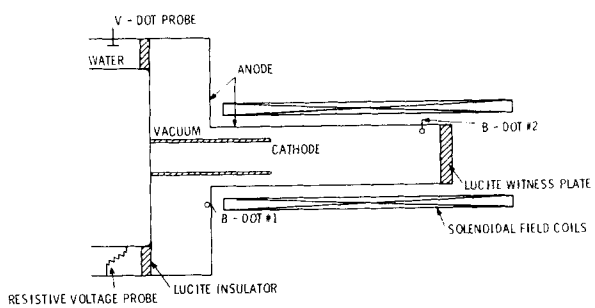

FIG. 7. Schematic layout of the Hydra experiments.

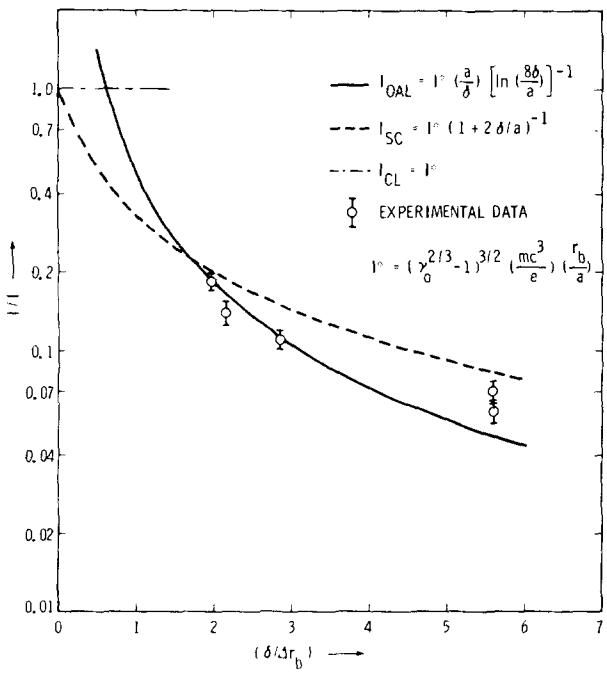

FIG. 8. Hydra smooth bore magnetron diode current variation with the parameter $(\delta/\Delta r_b)$ compared with various theoretical models.

axial gap follows the qualitative total current behavior presented in Fig. 3. For very small axial gaps the diode impedance is governed by the thickness of the beam and the separation distance between the beam and the *drift tube* wall. For very large axial gaps the impedance is determined by the beam thickness and its separation from the *diode* wall. For intermediate axial gaps the diode current will decrease with increasing gap separation, with the actual variation depending on the particular diode geometry.

B. Finite magnetic field effects

Relaxation of the very strong magnetic field assumption leads to at least two effects important in foilless diode design: 1. beam thickening due to non-zero Larmor orbits, and 2. radial oscillations of the beam envelope.

1. Beam thickness considerations

For large axial gaps ($L > R_D - r_2 = \delta^*$), or for geometries in which there is no axial gap ($R - r_2 = \delta$), the radial electric field due to the applied potential is of the order

$$E_r \sim \frac{\phi_0}{\delta^*}, \tag{16}$$

and the Larmor orbit radius is approximately

$$\Delta r_L \approx (2mc^2/e)(\phi_0/B_0^2\delta^*). \tag{17}$$

In the small gap limit the radial electric field is estimated according to the simple geometrical formula as

$$E_r \approx \phi_0 \frac{\delta}{L^2+\delta^2}, \tag{18}$$

and the orbit radius is given as

$$\Delta r_L \approx \frac{2mc^2}{e}\frac{\phi_0\delta}{B_0^2(L^2+\delta^2)}. \tag{19}$$

[When $L \sim \delta^*$, it is understood that the limiting expression for Eq. (19) is Eq. (17).]

If Δr_L becomes an appreciable fraction of the thickness a of the annular ring of the cathode over which field emission occurs, then the beam thickness will significantly vary with magnetic field strength. Since the diode current also depends on the beam thickness (the paramter a must be replaced by $\Delta r_b \approx a + \Delta r_L$), variations in the magnetic field strength will result in diode current variations. To illustrate this point, consider the small axial gap limit with $\delta \lesssim a$. In the limit of infinite magnetic field strength, an upper limit for the foilless diode current is calculated from Eq. (3) as

$$I_\infty \approx (\gamma_0^{2/3}-1)^{3/2}\frac{mc^3}{e}\frac{R}{a+2\delta}. \tag{20}$$

For finite magnetic fields the increase in diode current over that of Eq. (20) is

$$\Delta I_b \approx (\gamma_0^{2/3}-1)^{3/2}\frac{mc^3}{e}\frac{R}{a} \times\left\{\frac{a\Delta r_L}{(a+2\delta)(a+2\delta-\Delta r_L)}\right\}. \tag{21}$$

Writing $a = y$ and $\Delta r_L = x$, the expression in curly brackets becomes

$$\left\{\ \right\} = \frac{yx}{(y+2)(y+2-x)}.$$

This quantity is presented in Fig. 4 for various values of the parameter y over the allowed interval $0 \leqslant x \leqslant 1$. As x approaches unity the beam becomes thicker, but the beam-to-drift tube separation decreases. In this limit the diode current increases until $\Delta r_L > \delta$, and beam particles are lost to the drift tube wall.

2. Beam envelope behavior

By taking appropriate moments of the single-particle equations of motion, Lee and Cooper have derived a paraxial envelope equation that has considerable utility; their equation is[7]

$$\langle \ddot{r}\rangle + \frac{\dot{\gamma}}{\gamma}\langle \dot{r}\rangle + \frac{U}{\langle r\rangle} + \frac{\Omega_c^2}{4}\langle r\rangle = \frac{C^2}{\gamma^2\langle r\rangle^3}, \tag{22}$$

where $\langle r\rangle$ represents the rms beam radius and $\Omega_c = eB/\gamma m_0 c$. C^2 is a constant of integration determined from

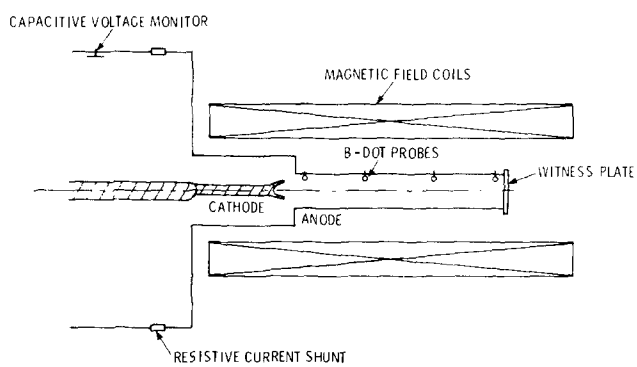

FIG. 9. FX-100 experimental diode schematic.

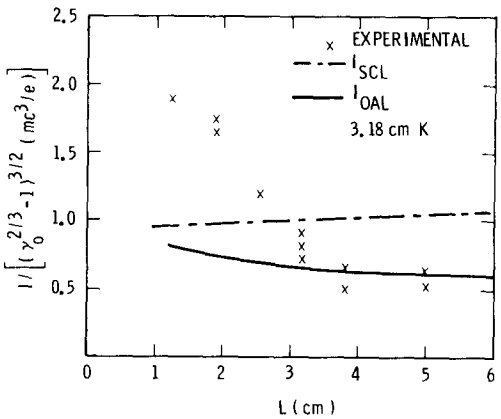

FIG. 10. Experimental beam current compared with the various theoretical estimates for the 3.18-cm hollow cathode.

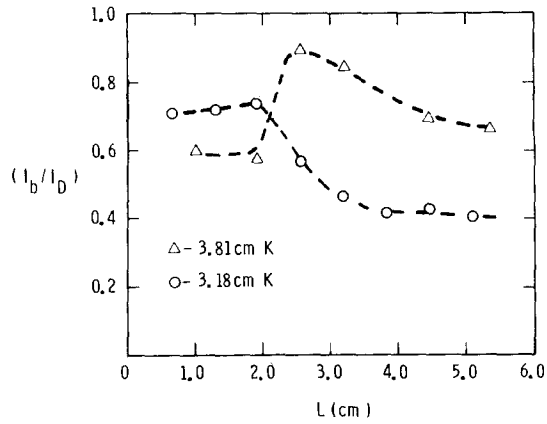

FIG. 11. Comparison of beam and diode currents as a function of axial gap separation for the 3.18- and 3.81-cm conical hollow cathode tips.

the initial conditions according to

$$C^2 = \left(\gamma^2\langle r\rangle^3\langle\ddot{r}\rangle + \frac{\dot{\gamma}}{\gamma}\langle\dot{r}\rangle + \frac{U}{\langle r\rangle} + \frac{\Omega_c^2}{4}\langle r\rangle\right)_0 . \quad (23)$$

The quantity U is the mean $\langle\omega_\beta^2 r^2\rangle$, where $\omega_\beta^2 = (e/\gamma m_0)[\beta B_\theta - E_r)/r]$ is the betatron frequency. For a thin hollow beam of thickness $a = r_2 - r_1$ and mean radius r_b, then $\langle r\rangle \simeq r_b$ and

$$\omega_\beta^2(r) \approx -\frac{2c^2}{\gamma^3 r_b^2}\frac{I_0}{mc^3/e}\frac{r-r_1}{a}, \quad (24)$$

where I_0 is the total current carried by the annulus after the beam velocity has become relativisitic. While thin hollow beams can have a very small spread in kinetic energy, it is apparent from Eq. (24) that phase mixing must eventually occur owing to betatron frequency spread across the annulus. Hence the results of this treatment are only valid for regions near the cathode where such phase mixing has not disrupted the laminar flow pattern of the beam.

In the thin beam limit,

$$\langle\omega_\beta^2 r^2\rangle \approx -\frac{c^2}{\gamma^3}\frac{I_0}{mc^3/e},$$

and Eq. (22) becomes

$$\ddot{r}_b + \frac{\dot{\gamma}}{\gamma}\dot{r}_b - \frac{c^2}{\gamma^3}\frac{I_0}{mc^3/e}\frac{1}{r_b} + \frac{\Omega_c^2}{4}r_b = \frac{C^2}{\gamma^2 r_b^3}. \quad (25)$$

Since the beam kinetic energy varies due to acceleration in the diode, Eq. (25) predicts radial oscillations of the beam envelope. Such oscillations are readily apparent in the sample 2-d (PIC) code calculation represented in Fig. 5. For this calculation a voltage of 2 MV was applied across the A-K gap, while a uniform B_z of 20 kG permeated the entire region. The electron trajectories shown in the figure are the r-z projections of the real 3-d orbits. For this case the space-charge-limited beam current was approximately 38 kA.

C. Parasitic losses

If lines of the external magnetic field connect regions on the cathode surface with regions on the anode surface, parasitic electron currents can cross the gap. Such currents load the diode without contributing useful beam current. To evaluate this effect it is necessary to consider electron motion in the radial electric, and longitudinal and azimuthal magnetic fields. The result of a detailed model, which includes the effects of space charge, indicates that parasitic losses should not be serious provided that[8]

$$\alpha^2\Delta \lesssim \frac{1}{3\pi}\frac{mc^2}{e}\frac{E_r B_\theta^3}{(B_z^2 + B_\theta^2)^{1/2}B_z^4}, \quad (26)$$

where Δ is the scale length of the region over which the component of the magnetic field normal to the cathode is nonvanishing, and α is the angle between the resultant magnetic field and the cathode surface.

The essential scaling indicated by Eq. (26) is

$$\alpha^2\Delta \lesssim k\,[\phi_0/(R - r_c)](I_s/r_c)^3 B_z^{-5},$$

where I_s is the current flowing in the shank of radius r_c, and ϕ_0 is the applied potential. Hence reducing the gap impedance should dramatically decrease the magnitude of the parasitic losses.

III. PRELIMINARY EXPERIMENTAL RESULTS

In the past the three foilless diode configurations of Fig.

TABLE I. Hydra smooth bore magnetron configuration.

Shot No.	V (MV)	B (kG)	r_c	Δr_b	δ	R	I_D (kA)	I_B (kA)
5927	1.2	8.6	4.45	0.30	1.59	6.03	160	20
5932	1.4	8.6	4.45	0.30	1.59	6.03	140	28.5
5944	1.0	8.6	5.08	0.48	0.95	6.03	185	27
5950	0.90	8.6	5.08	0.30	0.95	6.03	205	30

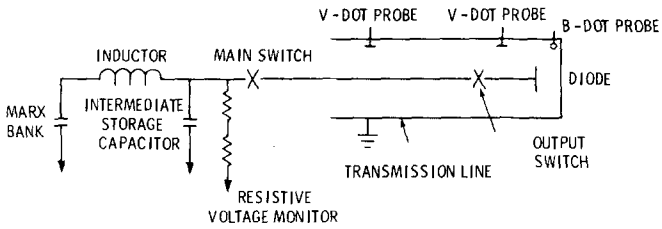

FIG. 12. High-current foilless diode generator schematic.

6 have received considerable attention.[3,9-13] The designs of Figs. 6(a) and 6(b) somewhat resemble the magnetron gun,[14] since the magnetic field of the external solenoid is approximately perpendicualr to the electric field in the diode region. The third configuration, Fig. 6(c), corresponds to a planar foilless diode in which the external magnetic field is approximately axially uniform, but is not necessarily oriented perpendicular to the accelerating electric field. Before proceeding with the design of the foilless diode, some operating experience with the various configurations was gained with two existing pulsers: (1) Hydra, a low-impedance water line,[15] and (2) the FX-100, an Ion Physics, Inc., Van de Graaff charged electron beam accelerator.

A. Hydra experiments

The schematic layout of the Hydra experiments is shown in Fig. 7. The diode voltage was determined using both a resistive and a capacitive monitor, while the diode current was measured with a resistive current shunt and an integrated B-dot loop. The beam current which transported to the end of the drift tube was measured with a second integrated B-dot loop. All electrical diagnostic signals were recorded using Tektronix 7912 transient digitizers. Lucite witness plates were used to determine the radial profile of the beam.

The axial magnetic field was provided by the discharge of an 80-kJ, 10-kV parallel capacitor bank through a solenoidal field coil; the peak field ($\sim$8.6 kG) was achieved in approximately 8 ms, allowing complete field penetration through the thin stainless steel drift tube. Triggering of Hydra was accomplished using the delayed trigger output of a Tektronix 555 oscilloscope used to monitor the current through the solenoid.

The first geometry explored with Hydra was essentially that of a smooth bore magnetron gun [Fig. 6(b)]. The experimental parameters for the various trials are presented in Table I. As indicated in the table (and for all Hydra trials), the total diode current (I_D) far exceeded the transported beam current (I_b), indicating substantial electron current loss in the diode. In Fig. 8 the transported beam current is compared with the various theoretical estimates as a function of the parameter ($\delta/\Delta r_b$), where Δr_b is the beam thickness as determined from the damage patterns on the lucite witness. For $(\delta/\Delta r_b) > 1.65$ the experimental data agree well with the OAL current expression, Eq. (6), while the space-charge-limit formula, Eq. (3), somewhat overestimates the beam current. The experimentally measured beam thickness data were observed to agree qualitatively with the simple estimate

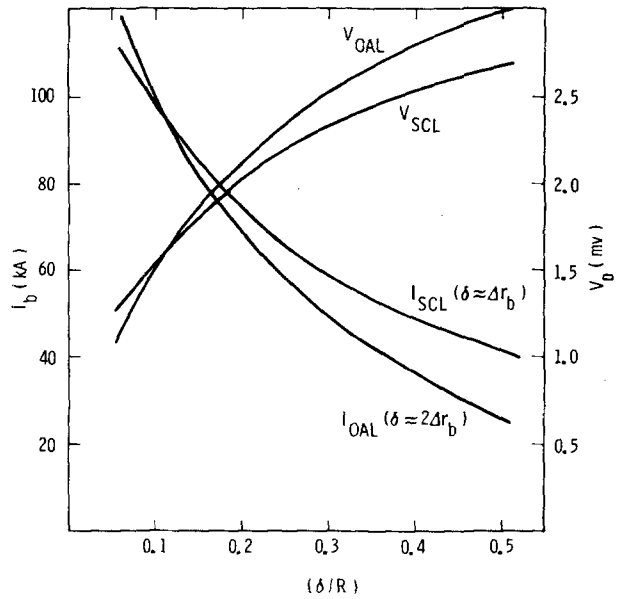

FIG. 13. Variation of foilless diode current and beam kinetic energy with the parameter (δ/R) for both the space-charge-limit and OAL approximations. Transmission line loading has been included assuming an initial charge voltage of 3.5 MV.

based on Larmor orbit theory after subtracting the zero-order thickness due to the cathode [Eq. (17)].

Experimental data could not be obtained for $(\delta/\Delta r_b) < 1.65$ owing to excessive parasitic losses and subsequent diode closure at the position of the field line intersection with the cylindrical anode; severe cathode damage was readily observed in these instances. In order to proceed, a different cathode design based on a variation of Fig. 6(c), but with a cathode tip diameter a factor of 2–3 times larger than the cathode shank diameter, was employed. This geometry permitted substantially longer pulse times without radial plasma closure; it also allowed the gap impedance to be varied by changing the axial gap separation. The beam currents obtained in this configuration were substantially higher (up to 80 kA). For small axial gap separations, the experimental data agreed with OAL predictions. For larger values of L, however, the data approached the OAL limit obtained by replacing δ with δ^*, the radial diode gap separation, as qualitatively predicted in Sec. II A 3.

B. FX-100 experiments

Based on the Hydra results, a variation of the planar foilless diode appeared to offer the required high beam currents, while the necessary control of the diode impedance could be achieved by simply varying the axial A-K gap separation. Moreover, the experimental results appeared to agree

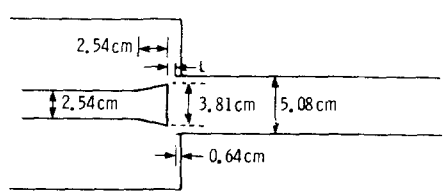

FIG. 14. Schematic design of the high-current foilless diode.

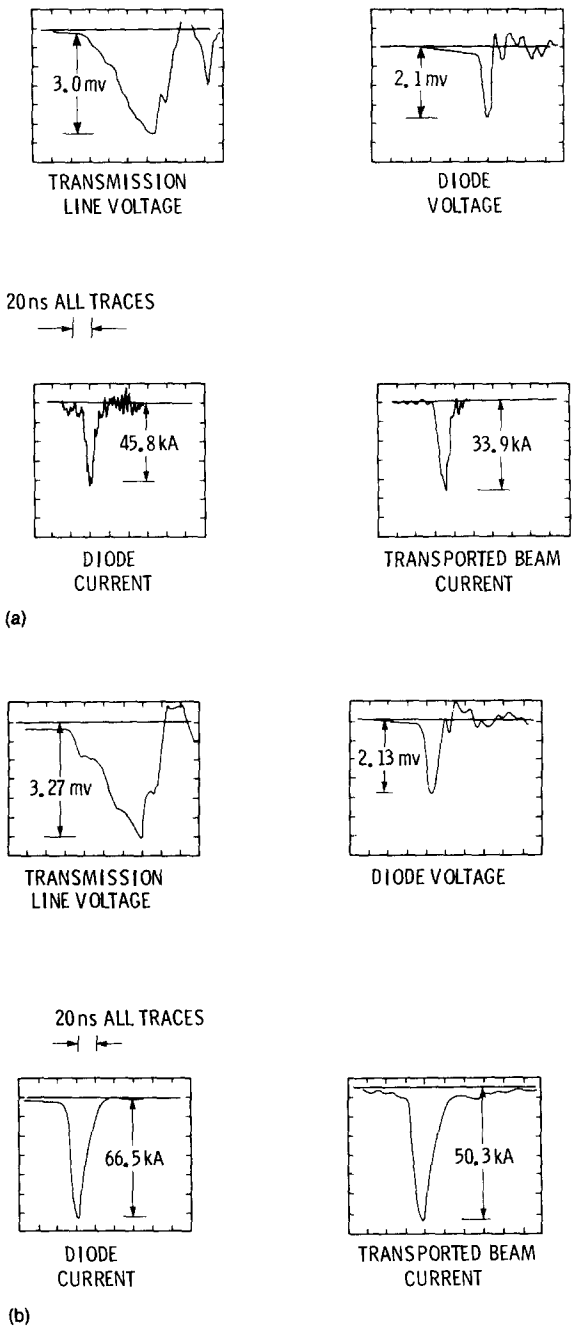

FIG. 15. Typical diagnostic signals for two different A-K axial gap separations. (a) A-K gap = 1.27 cm. (b) A-K gap = 0.80 cm.

rather well with theoretical predictions of the diode current and beam thickness. However, since no foilless diode designs could approach the very low impedance necessary for matching the Hydra water line, further experiments were conducted with the high-impedance FX-100 located at the Air Force Weapons Laboratory. The schematic layout for the FX-100 experiments is presented in Fig. 9.

The FX-100 consists of a Van de Graaff charged coaxial capacitor insulated with a high-pressure mixture of nitrogen and sulfur hexafluoride. For the data presented here the peak dc charge voltage was nominally 6 MV. Command triggering was achieved using the same technique as employed in the Hydra experiments. The diode voltage was monitored with a capacitive-voltage divider, while the total diode current was recorded with a resistive current shunt. The beam current was monitored with four integrated B-dot loops distributed axially along the drift tube; the transported beam current was monitored with a Faraday cup, while the beam thickness was monitored by vaporizing thin (0.0025 cm) aluminum foils. The peak magnetic field available (8.6 kG) was obtained using the same hardware employed in the Hydra experiments.

Significant beam data were taken for two different conical cathode tips of outer diameter 3.18 and 3.81 cm. For both hollow tips the beam thickness estimate agrees well with the data for small values of the parameter $\delta\,(L^2+\delta^2)^{-1}$, but rather badly underestimates the beam thickness in the small L limit. This discrepancy could result from a number of effects, including (1) variations in beam parameters over the pulse time, (2) mixing of the radial oscillations of the beam envelope, and (3) unaccounted-for variations in the radial electric field as the beam expands and nears the drift tube wall.

In Fig. 10 the measured beam currents from the 3.18-cm cathode are compared with the various theoretical estimates. In the large L limit the data is in excellent agreement with the OAL estimate, while the space-charge-limit expression considerably overestimates the observed current levels. As L is decreased below ~ 3 cm, however, the experimental results substantially deviate from all models. Since the beam currents exceed even the space-charge limit (using the witness plate beam thickness data), these results tend to suggest that the actual beam thickness at the time of peak current is somewhat different than that obtained from the witness plate data which is integrated over the pulse time. It is further possible that the beam is highly nonuniform over the width of the annulus. For the 3.81-cm cathode the basic assumption of the OAL formula, Eq. (6), is violated ($\delta/a \lesssim 1$). In this case the space-charge-limiting current formula, Eq. (1), predicts the observed currents rather well.

The ratio of the transported current I_b to the total diode current I_D, as measured by the resistive current shunt, is

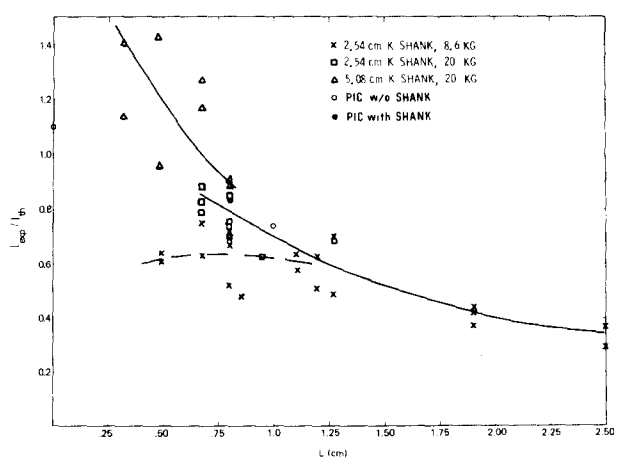

FIG. 16. A comparison of the experimentally measured foilless diode beam current with the $L = 0$ OAL estimate as a function of axial gap separation. PIC points are from two-dimensional particle-in-cell computer simulations.

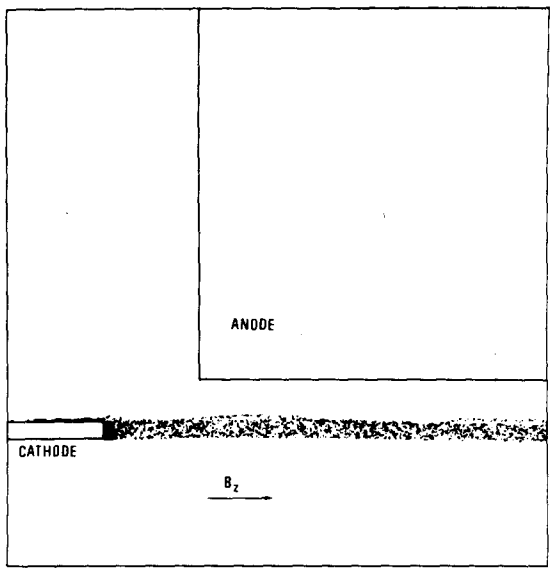

FIG. 17. Computer simulation of the foilless diode including the effects of shank emission. $V_D = 2.0$ MV, $B_0 = 18$ kG, $L = 0.8$ cm, $a = 0.24$ cm, and $I_b \simeq 43$ kA. A steady-state electron map is shown.

displayed in Fig. 11 for the two different cathode tip sizes. [Unfortunately, the cathode tip angle α was much too large to compare our data with the theoretical prediciton, Eq. (26)]. For the case of the smaller tip, I_b/I_D increased as the axial gap separation was decreased to ~ 2.0 cm, and remaiend reltively constant at approximately 70% thereafter. For the larger tip, the same variation with gap spacing was noted for $L > 2.5$ cm and ratios of 90% were attained at $L \simeq 2.5$ cm; however, for $L < 2.5$ cm, very much lower values of I_b/I_D were obtained. These results suggest that parasitic losses can be minimized by decreasing the gap impedance (small L, beam close to wall), provided the beam does not strike the drift tube wall (large cathode–small gap data).

IV. HIGH CURRENT FOILLESS DIODE ACCELERATOR DESIGN

A. Design procedure

Based on the Hydra and FX-100 experimental data and the theoretical analyses, the design of the high-current foilless diode accelerator was developed using the following procedure: first, assuming no parasitic currents, the diode current formulas were used in conjunction with the load line of the injector transmission line to establish an approximate diode geometry. Using this approximate design the necessary magnetic field strength required to maintain a thin beam was then determined. Second, the diode was constructed and used to evaluate diode performance, including parasitic losses.

The major components of the accelerator are a Marx generator, an intermediate storage capacitor (ISC), a 20-Ω oil-dielectric pulse-forming transmission line (PFL), and the foilless diode as indicated in Fig. 12. The 3-MV Marx generator charges the ISC in 1.5 μs. When the self-break, SF_6 spark gap closes, the ISC charges the 50-cm diameter PFL to 3.5 MV in approximately 100 ns. This rapid charge allows high operating electric fields (460 kV/cm) in the PFL, and ensures reliable low-jitter (~ 1 ns) operation of the self-break, multichannel, oil-dielectric spark gap switches.[16] Six point-plane switches, rather than blade-plane switches, are used in this design for ease of mechanical construction. The diode current risetime indicates that at least four channels close on each shot.

The diode voltage is determined by the break point of the PFL switches and the loading of the PFL by the diode impedance according to

$$V_D = V_0 - ZI_D. \tag{27}$$

In Eq. (27) V_0 is the break-point voltage of the output switch; Z is the characteristic impedance of the transmission line; V_D and I_D are the diode voltage and current, respectively. Hence a 20-Ω PFL charged to 3.5 MV is capable of providing the nominal desired diode operating parameters (2 MV, 75 kA).

Assuming $V_0 = 3.5$ MV and $Z = 20\,\Omega$, the variation of diode current and beam kinetic energy with the ratio δ/R is presented in Fig. 13 for both the OAL approximation and the space-charge limit, Eqs. (6) and (3). For the nominal design goals of 2 MV, 75 kA, the appropriate range for δ/R is 0.16–0.2. Fixing the drift tube radius at $R = 2.54$ cm, δ falls in the range 0.41–0.51 cm, and the outer radius of the beam should fall in the range 2.03–2.13 cm. The selected value of r_c was 1.91 cm, while the thickness a of the cathode emission surface was chosen to be 0.16 cm. Assuming Larmor orbits also of the order 0.16 cm implies an outer beam radius of 2.05 cm in the desired range. The magnetic field strength required to maintain Δr_L at 0.16 cm is 15 kG, assuming $R - r_c = 0.63$ and $a = 0.16$ cm for a diode voltage of 2 MV. A schematic of the diode constructed on the basis of these arguments is shown in Fig. 14. The axial gap separation L and the magnitude of the magnetic field strength could be easily varied for adjustment purposes.

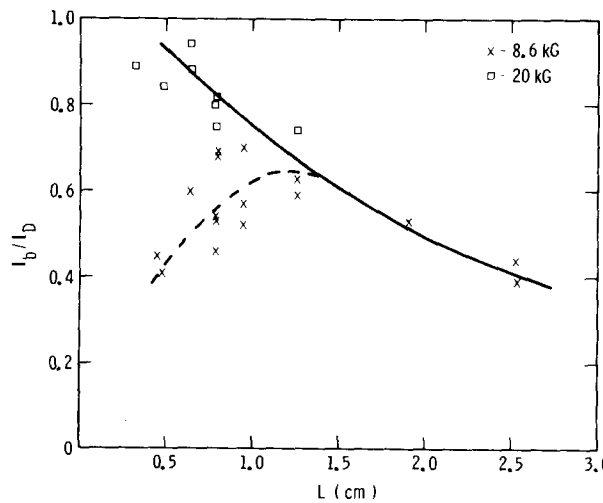

FIG. 18. The ratio of the transported beam current I_b to the total diode current I_D as a function of axial gap separation for two different values of magnetic field strength.

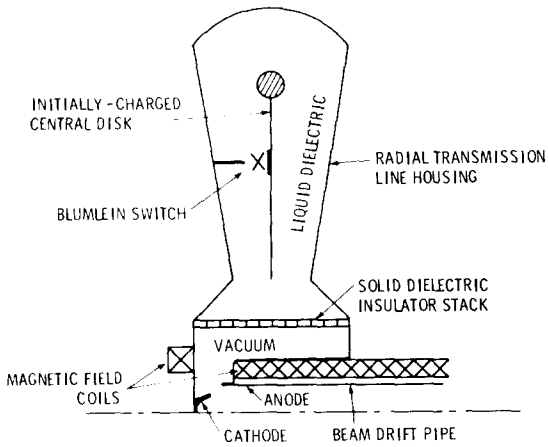

FIG. 19. Schematic design for a foilless diode driven by a Blumlein-configured radial transmission line.

B. Experimental checkout

Typical voltage and current diagnostic signals are presented in Fig. 15 for two different values of axial gap separation. At the smaller axial gap spacing, substantial (~ 5 kA) prepulse current was measured by both the diode and the Farady cup current monitors. For the larger gap, the prepulse current was substantially reduced, but the diode signals were typically much noisier, perhaps owing to the larger percentage of parasitic current flow.

A comparison of the experimentally measured foilless diode beam current with the $L = 0$ OAL limit [Eq. (17) using the estimated beam thickness] is presented in Fig. 16 as a function of axial gap separation for two values of the external field strength and two different cathode shanks. Periodic checks of the beam thickness using lucite witness plates indicated reasonable agreement with the calculated values, especially at the larger field strengths.

For the largest axial gaps, the measured beam currents were substantially below the $L = 0$ OAL estimates in qualitative agreement with the arguments presented in Section II A 3. The agreement is not quantitative, however, indicating that a more careful treatment of 2-d geometry effects is required to adequately predict the diode impedance variation with axial gap separation. For the smaller gap separation, the experimental data agree well with the OAL estimate for the case of the stronger magnetic field. At the lower field level the beam thickness somewhat exceeded the Larmor orbit prediction leading to the observation of less current. A few trials were also performed with a cathode shank diameter which exceeded the diameter of the conical cathode tip. Although the shank was rounded, currents in excess of the theoretical limit were measured, indicating some emission current from the shank contributed to the beam current. Also shown for comparison are the results of various computer simulations (one of which is shown in Fig. 17). In general, the agreement between the computer simulations and the experimental results for various axial gaps is quite good. In addition, when the axial gap is reduced to zero, the computer simulation closely agrees with the OAL estimate.

In a few trials the stainless steel cathode tip was sprayed with carbon aerosol and the transported beam current was observed to decrease by 10%–15%. It is suspected that the carbon coating may have resulted in electron emission from interior regions of the tip, thereby reducing the total space-charge-limited current.

The ratio of the transported beam current I_b to the total diode current I_D for the various cases listed above is displayed in Fig. 18. As observed with the FX-100, parasitic losses can be minimized provided that the axial gap is small (decreased geometrical impedance). The increased beam current losses observed at the lower magnetic field strength are believed to result from substantial beam thickening (lower space-charge limit), and possibly to loss of beam particles to the drift tube wall.

V. SUMMARY

Based on the experimental work reported here, the following important conclusions pertaining to planar foilless diodes can be summarized.

(1) For thin hollow beams, if the ratio of the beam separation from the drift tube wall to the beam thickness $\delta/\Delta r_b$ exceeds approximately 1.65, then the approximate OAL expression is a good estimate for the observed beam current; in the opposite limit, the OAL expression overestimates the beam current and the appropriate thin beam space-charge-limit formulas give a better estimate.

(2) For relatively thin beams, $\Delta r_b/r_b \sim 0.1$, the beam thickness to be used in the diode current formulas is essentially determined by the cathode tip geometry and the single-particle Larmor orbits, accounting for two-dimensional electric field effects in the cathode-anode gap region.

(3) For small axial gaps $L < \delta^*$, where δ^* is the radial separation from the cathode to the diode wall, variations in the axial gap separation affect the diode impedance primarily through variations in the beam thickness. As L increases to δ^*, the diode impedance increases and tends to approach the OAL estimate with δ replaced by δ^*.

(4) Parasitic current losses due to electrons crossing the diode by following magnetic field lines in a direction opposite to that of the primary electron flow are a serious problem because of the diode loading effect. In the standard foilless diode configuration, such losses can be minimized by decreasing the geometrical gap impedance.

The foilless diode design described in this paper routinely produces 2-MeV electron beam curents of 65–70 kA, with $\Delta r_b/r_b \approx 0.1$ and $r_b \approx 2$ cm in a drift tube of radius $R \approx 2.5$ cm. The operating axial magnetic field strength is approximately 20 kG. Parasitic current losses have been reduced to $\sim 10\%$ of the total diode current. The remaining losses may be due to a loss of magnetic insulation along regions of the cathode shank where fringing of the external magnetic field occurs.[17]

For future injector development a foilless diode driven by a radial pulse line structure in a Blumlein switch configuration merits consideration (see Fig. 19). Use of the radial line design[18] completely eliminates prepulse voltage on the diode, while the Blumlein configuration produces a unipolar

pulse equal to the charge voltage for a matched diode load. Further, elimination of the cathode shank structure should reduce parasitic electron losses to a negligible value.

ACKNOWLEDGMENTS

The authors thank A. W. Sharpe and L. E. Stevenson for their experimental assistance and numerous helpful suggestions. We also acknowledge the support and encouragement of G. Yonas. This work was jointly sponsored by the U.S. Department of Energy and the Air Force Weapons Laboratory.

[1]R. B. Miller and D. C. Straw, J. Appl. Phys. **47**, 1897 (1976).
[2]L. S. Bogdankevich and A. A. Rukhadze, Sov. Phys. Usp. **14**, 163 (1971).
[3]M. Friedman and M. Ury, Rev. Sci. Instrum. **41**, 1334 (1970).
[4]The highest current densities in the literature are 40–50 A/cm^2, reported by M. I. Avramenko, V. A. Głukhikh, O. A. Gusev, E. G. Komar, O. L. Komarov, V. S. Kusnetsov, A. S. Perlin, and M. P. Svinin, Sov. Phys. Tech. Phys. **19**, 368 (1974).
[5]E. Ott, T. M. Antonsen, Jr., and R. V. Lovelace, Phys. Fluids **20**, 1180 (1977).
[6]J. Chen and R. V. Lovelace, Phys. Fluids **21**, 1623 (1978).
[7]E. P. Lee and R. K. Cooper, Part. Accel. **7**, 83 (1976).
[8]N. F. Kovalev, V. E. Nechaev, M. I. Petelin, and M. I. Fuks, Sov. Tech. Phys. Lett. **3**, 168 (1977).
[9]M. Friedman and D. A. Hammer, Appl. Phys. Lett. **21**, 174 (1972).
[10]A. A. Kolomenskii, E. G. Krastelev, and B. N. Yablokov, Sov. Tech. Phys. Lett. **2**, 104 (1976).
[11]I. Z. Gleizer, A. N. Didenko, A. G. Zherlitsyn, Ya. E. Krasik, Yu. P. Usov, and V. I. Tsvetkov, Sov. Phys. Lett. **1**, 214 (1975).
[12]L. A. Zubkov, A. A. Kolomenskii, E. G. Krastelev, A. M. Maine, V. A. Papadichev, and S. G. Rott, Sov. Tech. Phys. Lett. **2**, 265 (1976).
[13]J. A. Nation and M. Read, Appl. Phys. Lett. **23**, (1973).
[14]G. S. Kino and N. Taylor, Trans. IRE **ED-9**, 1 (1962).
[15]T. H. Martin, IEEE Trans. Nucl. Sci. **NS-20**, 289 (June 1973).
[16]D. L. Johnson, Proceedigns of the International Conference on Energy Storage, Compression and Switching, Asti-Torino, Italy, November 1974, p. 515 (unpublished).
[17]M. Mostrum, Proceedings of the 2nd IEEE International Pulsed Power Conference, Lubbock, Tex., June, 1979 (to be published).
[18]A. I. Pavloskii, V. S. Bosamykin, G. D. Kuleshov, A. I. Gerasimov, V. A. Tananakin, and A. P. Klementev, Sov. Phys. Dokl. **20**, 441 (1975).